

# A New Photometric Model of the Galactic Bar using Red Clump Giants

Liang Cao<sup>1</sup>, Shude Mao<sup>1,2</sup>, David Nataf<sup>3,4</sup>, Nicholas J. Rattenbury<sup>2</sup>, Andrew Gould<sup>4</sup>

<sup>1</sup> *National Astronomical Observatories, 20A Datun Road, Chinese Academy of Sciences, Beijing, 100012, China*

<sup>2</sup> *Jodrell Bank Centre for Astrophysics, The University of Manchester, Alan Turing Building, Manchester M13 9PL, UK*

<sup>3</sup> *Research School of Astronomy and Astrophysics, Australian National University, Canberra, ACT 2611, Australia*

<sup>4</sup> *Department of Astronomy, The Ohio State University, 140 West 18th Ave., Columbus, OH 43210, USA*

Accepted ..... Received ..... ; in original form.....

## ABSTRACT

We present a study of the luminosity density distribution of the Galactic bar using number counts of red clump giants (RCGs) from the OGLE-III survey. The data were recently published by Nataf et al. (2013) for 9019 fields towards the bulge and have  $2.94 \times 10^6$  RC stars over a viewing area of  $90.25 \text{ deg}^2$ . The data include the number counts, mean distance modulus ( $\mu$ ), dispersion in  $\mu$  and full error matrix, from which we fit the data with several tri-axial parametric models. We use the Markov Chain Monte Carlo (MCMC) method to explore the parameter space and find that the best-fit model is the  $E_3$  model, with the distance to the GC is 8.13 kpc, the ratio of semi-major and semi-minor bar axis scale lengths in the Galactic plane  $x_0, y_0$ , and vertical bar scale length  $z_0$ , is  $x_0 : y_0 : z_0 \approx 1.00 : 0.43 : 0.40$  (close to being prolate). The scale length of the stellar density profile along the bar's major axis is  $\sim 0.67$  kpc and has an angle of  $29.4^\circ$ , slightly larger than the value obtained from a similar study based on OGLE-II data. The number of estimated RC stars within the field of view is  $2.78 \times 10^6$ , which is systematically lower than the observed value. We subtract the smooth parametric model from the observed counts and find that the residuals are consistent with the presence of an X-shaped structure in the Galactic centre, the excess to the estimated mass content is  $\sim 5.8\%$ . We estimate the total mass of the bar is  $\sim 1.8 \times 10^{10} M_\odot$ . Our results can be used as a key ingredient to construct new density models of the Milky Way and will have implications on the predictions of the optical depth to gravitational microlensing and the patterns of hydrodynamical gas flow in the Milky Way.

**Key words:** Galaxy - structure: Galaxy - stellar content - Galaxy: bulge - Galaxy: centre

## 1 INTRODUCTION

Most spiral galaxies in the local Universe are barred. Galactic bars are often straight and their presence appears to be intimately related to star formation. Rings are often seen in these galaxies and they are likely related to resonances in a rotating barred potential. Thus barred galaxies offer exciting opportunities to understand gas and dynamical processes in spiral galaxies (see e.g. Sellwood & Wilkinson 1993; Athanassoula 2012 for reviews). It is now generally accepted that the inner region of our own Galaxy also hosts a tri-axial, bar-like structure. Observational evidence for a bar has arisen from several sources, such as the studies of gas kinematics (e.g. Binney et al. 1991), surface brightness (e.g. Blitz & Spergel 1991), star counts (e.g. Nakada et al. 1991; Stanek et al. 1994) and microlensing (e.g. Udalski et al. 1994; see Gerhard 2002 for a review).

Various tracers have been used to constrain stellar density models of the inner Galaxy. Dwek et al. (1995) used the COBE-DIRBE multi-wavelength observations of the Galactic centre (Weiland et al. 1994) to constrain several multi-parameter analytic bar models. Stanek et al. (1997) first used red clump giants (RCGs) to constrain bar models (see also Babusiaux & Gilmore

2005 and Nishiyama et al. 2005 who traced the bulge RCG population in the infrared). Rattenbury et al. (2007) applied the method of Stanek et al. (1997) to OGLE-II data and updated the bar parameters using the RCG population.

Unfortunately these studies leave many bar parameters uncertain. This may reflect the intrinsic complexities of the Galactic bar. For example, there has been a fair amount of discussion about the existence of a nuclear bar. Nishiyama et al. (2005) found a clear change of slope in the red clump giants around  $|l| = 4^\circ$ , which was confirmed recently by the VVV survey (Gonzalez et al. 2011). This was interpreted as the existence of a nuclear bar. However, numerically simulated bars appear to be able to reproduce the changes in the slope without any nuclear structure (Gerhard & Martinez-Valpuesta 2012). With more and more dynamical data emerging from several kinematic surveys (e.g., BRAVA, Howard et al. 2008, ARGOS, Freeman et al. 2013, and APOGEE, Nidever et al. 2012), it appears increasingly important to construct a more accurate photometric model, which will serve as a key ingredient in self-consistent dynamical modelling (Wang et al. 2012; Long et al. 2013).

The outline of this paper is as follows. In §2 we summarize the observational data used, as released by Nataf et al. (2013); in §3 we describe the methodology used in this analysis; in §4, we apply our methods to the OGLE-III data, and present the main results of this work. In §5 we discuss our results and compare them with earlier work.

## 2 DATA SAMPLE

In this paper, we explore the OGLE-III observation data recently published by Nataf et al. (2013) who carefully studied the extinction and the red clump giant population using both OGLE and 2MASS data. The RC is a prominent, well-populated, and localized feature of Galactic bulge CMDs (Terndrup et al. 1998; Stanek et al. 1994). RCGs are very good standard candles with  $M_I = -0.12$  and an intrinsic dispersion of 0.09 mag in luminosity at the estimated age and metallicity distribution of the bulge stellar population (Nataf et al. 2013). A more detailed discussion of the effect of metallicity can be found in §4.4.

The final data of Nataf et al. (2013) contain 9019 sightlines, which are almost entirely within the range  $-10^\circ < l < 10^\circ$  and  $2^\circ < |b| < 7^\circ$  and have a sky coverage of  $90.25 \text{ deg}^2$ . The catalogue contains the total number counts, mean distance modulus, geometrical variance, i.e. square of the dispersion in distance modulus, and full error matrix for each sightline, which come from the extinction maps.

These new data address two shortcomings in the study by Rattenbury et al. (2007). First, the total area in Rattenbury et al. (2007) covered only about 11 square degrees, spread over a longitude range of  $-6.8^\circ \leq l \leq 10.6^\circ$  degrees. Furthermore, the field latitudes are clustered around  $(-4^\circ)$  with only three fields at positive latitudes. Second, more seriously, Rattenbury et al. (2007) found that in order to match the luminosity of local and bulge red clump giants, an offset of 0.3 magnitude had to be artificially applied. The study by Nataf et al. (2013) addressed both issues. First, they resolve the “offset” difficulty by a much more careful consideration of extinction and a new calibration in the intrinsic luminosity of the red clump giants. Second, the field covers larger than 90 square degrees, nearly one order of magnitude larger than that used in Rattenbury et al. (2007). As a result, the differences between different models become much more drastic and the constraints on the model parameters are tighter. The data also allow us to explore the residuals between data and model much more convincingly, which we will exploit in some detail (see §4).

## 3 METHODOLOGY

In this section, we first describe the parametric tri-axial models we use to model the luminosity density model of the Galactic bar, then we outline the Markov Chain Monte Carlo method we use to find the best-fit parameters for each model. The results of our procedure will be presented in the next section.

### 3.1 Parametric models

We first re-examine a few models of bar density distribution proposed by Dwek et al. (1995):

$$n_{G_1} = N_0 \exp(-r^2/2), \quad (1)$$

$$n_{E_2} = N_0 \exp(-r), \quad (2)$$

$$n_{E_3} = N_0 K_0(r_s), \quad (3)$$

where  $K_0$  is the modified Bessel function of the second kind and

$$r = \left[ \left( \frac{x}{x_0} \right)^2 + \left( \frac{y}{y_0} \right)^2 + \left( \frac{z}{z_0} \right)^2 \right]^{1/2} \quad (4)$$

$$r_s = \left[ \left[ \left( \frac{x}{x_0} \right)^2 + \left( \frac{y}{y_0} \right)^2 \right]^2 + \left( \frac{z}{z_0} \right)^4 \right]^{1/4}. \quad (5)$$

These models are representative of a larger suite of parametric models studied by Rattenbury et al. (2007).

We set the origin of the coordinate system at the Galactic Centre (GC), with the x-y plane aligned with the mid-plane of the Galaxy and the z-direction parallel to the direction of the Galactic poles. The x-direction is defined to be co-linear with the semi-major axis of the bar. The functions are rotated by an angle  $\alpha$  around the z-axis.  $N_0$  is the number counts per  $\text{kpc}^3$ , and the distance to the GC is another free parameter  $R_0$ . Thus we have six parameters to model the bar structure.

The bar can also be rotated by a tilt angle  $\beta$  around the  $y$  axis, corresponding to the Sun's position away from the mid-plane of the Galaxy. Many previous studies found that the angle  $\beta$  is close to zero (Rattenbury et al. 2007; Robin et al. 2012), nevertheless we include it as a seventh model parameter as a test. Furthermore, there is tentative evidence that the centroid of the bar may be offset from the centre of the Galaxy (as evidenced, for example, from the possible gamma-ray line emission offset from the centre, see Su & Finkbeiner 2012). Thus we also check the importance of two additional offset parameters,  $\delta l$ ,  $\delta b$ . Finally, we also test the case for which both the tilt angle and the centre offset are included. We therefore fit the data using models in which all six, seven, eight or nine parameters are allowed to vary and compare the results with those found using the simplest six-parameter model.

With these models, we can calculate analytically the number counts, mean distance modulus and geometrical variance of each sightline as derived by Nataf et al. (2013).

The number counts in each sightline  $N_i$  is:

$$N_i = c_i \Delta\Omega \int_{s_{\min}}^{s_{\max}} n(s) s^2 ds, \quad (6)$$

Where  $\Delta\Omega$  is the solid angle subtended around each sightline, and  $c_i$  is assumed to be a constant. We discuss the effects of metallicity on  $c_i$  in §4.4.  $s_{\min}$  and  $s_{\max}$  are the minimum and maximum distances along the line of sight. We take  $s_{\min} = 3$  kpc and  $s_{\max} = 13$  kpc. We perform the integration over the range of  $\sim R_0 \pm 5$  kpc as we do not expect the tri-axial bulge density structure to exceed these limits. The results are insensitive to the choice of integration limits since the bar density falls away rapidly and the contribution to the integral over the outer part of the bulge is negligible. Taking  $\sim R_0 \pm 3$  kpc instead, the total number count changes only by 0.2% on average, and thus has the integration limit has little effect on our results.

The mean distance modulus of each sightline  $\mu_i$  can be calculated as:

$$\mu_i = \int_{s_{\min}}^{s_{\max}} n(s) s^2 \mu ds / \int_{s_{\min}}^{s_{\max}} n(s) s^2 ds, \quad (7)$$

where the distance modulus is  $\mu = 5 \log(s/\text{kpc}) + 10$ .

The geometrical variance  $\sigma_{\mu,i}$  can be written as,

$$\sigma_{\mu,i}^2 = \left[ \int_{s_{\min}}^{s_{\max}} n(s) s^2 \mu^2 ds / \int_{s_{\min}}^{s_{\max}} n(s) s^2 ds \right] - \mu_i^2, \quad (8)$$

We can evaluate the  $\chi^2$  goodness-of-fit statistic using the number counts, mean distance modulus, geometrical variance, and their covariance matrix. The  $\chi^2$  of the bar model can be written as,

$$\chi^2 = \sum_i (\mathbf{X}_i^{\text{mod}} - \mathbf{X}_i^{\text{obs}})^T \mathbf{S}_i^{-1} (\mathbf{X}_i^{\text{mod}} - \mathbf{X}_i^{\text{obs}}). \quad (9)$$

$\mathbf{X}_i^{\text{mod}}$  comprises the number counts ( $N_i$ ), mean distance modulus ( $\mu_i$ ) and geometrical variance ( $\sigma_{\mu,i}^2$ ) for the  $i$ -th sightline for the model under consideration, while  $\mathbf{X}_i^{\text{obs}}$  comprises the observed values of these variables for the same sightline.  $\mathbf{S}_i$  is the covariance matrix of uncertainties. The data comprising  $\mathbf{X}_i^{\text{mod}}$  are available from Nataf et al. (2013) and include 9019 lines of sight in total.

### 3.2 Markov Chain Monte Carlo search for best-fit models

For each of the parametric models, there are at least six parameters to constrain. We use Bayesian inference to provide a probabilistic distribution of tri-axial bar model parameters by combining prior information with the data. Information from the data and prior knowledge entirely determines the posterior probability distribution as follows:

$$\pi(x) \propto \mathcal{L}(\text{data}|x) \times \text{prior}(x). \quad (10)$$

We use Markov Chain Monte Carlo (MCMC) simulations to explore the parameter space and find the posterior distribution. MCMC can be implemented in a number of ways to explore the parameter space. In this work we use the standard

Model	$R_0$ (kpc)	$x_0$ (kpc)	$y_0$ (kpc)	$z_0$ (kpc)	$\alpha$ (deg)	$\delta l$ (deg)	$\delta b$ (deg)	$\beta$ (deg)	$\chi_1^2$	$\chi_2^2$	$\chi_3^2$	$\chi_4^2$	$\chi^2/d.o.f$
$G_1$	8.19	1.18	0.49	0.42	30.7				24160	33867	27850	7377	3.45
$E_2$	8.16	0.66	0.27	0.25	32.4				17094	31782	17842	3681	2.60
$E_3$	8.13	0.67	0.29	0.27	29.4				15675	31488	15989	1060	2.37
$G'_1$	8.22	1.18	0.49	0.42	30.7			-6.97	23897	33668	27880	7073	3.42
$E'_2$	8.18	0.67	0.27	0.25	32.3			-14.0	17126	31396	17851	3319	2.58
$E'_3$	8.13	0.67	0.29	0.27	29.4			0.11	15675	31482	15989	1066	2.37
$G''_1$	8.25	1.19	0.50	0.42	30.9	-0.38	-0.013		23285	33950	27781	5922	3.36
$E''_2$	8.20	0.69	0.27	0.25	32.5	-0.27	-0.024		16965	31822	17768	2445	2.55
$E''_3$	8.15	0.68	0.29	0.27	29.5	-0.10	-0.034		15787	31488	15906	674	2.36
$G'''_1$	8.25	1.19	0.50	0.42	30.9	-0.35	-0.016	-2.02	23319	33817	27800	5939	3.36
$E'''_2$	8.20	0.67	0.27	0.25	32.5	-0.22	-0.031	-6.67	17058	31528	17774	2469	2.54
$E'''_3$	8.15	0.68	0.29	0.27	29.5	-0.11	-0.034	0.59	15797	31459	15904	686	2.36

**Table 1.** The best fit values of six, seven, eight and nine-parameter tri-axial galactic bar models. The  $\chi^2$  contributed from the number counts ( $\chi_1^2$ ), mean distance modulus ( $\chi_2^2$ ), geometrical variance ( $\chi_3^2$ ) and the non-diagonal terms in the error matrix ( $\chi_4^2$ ) are also listed.

random walk Metropolis-Hastings algorithm (Metropolis et al. 1953; Hastings 1970). At any point  $x_n$  in the chain we generate a new trial point  $x_{\text{trial}}$  by drawing parameter shifts from the symmetrical proposal distribution function  $\phi(x - x_n)$ . This algorithm is universal for any proposal distribution function. Here, we use a multi-dimensional Gaussian distribution in the vector of parameters. We accept a candidate state  $x_{n+1}$  with probability  $\min\{1, \pi(x_{\text{trial}})/\pi(x_n)\}$ , where  $\pi(x)$  is the equilibrium distribution of the chain (Lewis & Bridle 2002).

For each model, the chain is started at the corresponding best-fit model values of parameter vector as given in Rattenbury et al. (2007). The model total star counts are normalised so that they reproduce the observed  $N_0$  for each sightline. The MCMC simulation is then allowed to run, varying each of the six parameters in the range of [8.0, 8.5] (kpc), [0.0, 2.0] (kpc), [0.0, 1.0] (kpc), [0.0, 1.0] (kpc), [20.0, 40.0] (deg), [0.0,  $2.0 \times 10^7$ ] ( $\text{kpc}^{-3}$ ) for  $R_0, x_0, y_0, z_0, \alpha, N_0$  respectively. Given the sampling strategy described above, we also use an adaptive step size to guarantee a sufficient sampling of the posterior, leading to convergence to the equilibrium posterior distribution in the chain after several thousand steps. We terminate the chains for each model according to its variance in the sample mean ( $\sigma_{\bar{x}}^2$ ) characterized by the dimensionless ratio  $\sigma_{\bar{x}}^2/\sigma_0^2$  where  $\sigma_0^2$  is the variance of the underlying distribution for convergence diagnostics (Dunkley et al. 2005). We neglect the first half of the chain to avoid the influence of initial conditions, and then obtain the posterior distribution of the parameters.

## 4 RESULTS

For the simple bar models, we have six parameters  $R_0, N_0, x_0, y_0, z_0$  and  $\alpha$ . We measure  $2.94 \times 10^6$  RC stars in the OGLE-III data over an area of  $90.25 \text{ deg}^2$ . The total number of sightlines is 9019. For each model, we run the MCMC chains and obtain the posterior distribution of each parameter and its best fit value for each model.

The results of best fit parameters are presented in Table 1. Since  $N_0$  does give the normalization for the total number of RC stars in the bulge, but it doesn't effect the spatial distribution of the model. Thus we include  $N_0$  in the MCMC chain but do not give its value here. We separate  $\chi^2$  contributions from the number counts ( $\chi_1^2$ ), mean distance modulus ( $\chi_2^2$ ), geometrical variance ( $\chi_3^2$ ) respectively.  $\chi_4^2$  is the contribution from non-diagonal terms in the error matrix. Among these models, the  $E_3$  model has the smallest  $\chi^2/d.o.f$  values and the  $G_1$  model has the largest  $\chi^2/d.o.f$ . This suggests that the  $E_3$  model best fit the data, while the  $G_1$  model fits the data worst.

We present the marginalized posterior distribution of the parameters for the six-parameter  $E_3$  model in Fig. 1. We can see that the probability distribution function (PDF) of each parameter is nearly Gaussian. We also show the degeneracy between each parameter in Fig. 1. The 1- and 2- $\sigma$  regions (i.e., 68% and 95% confidence levels) are shown in inner and outer contour lines respectively.

We compare the model prediction quantities, e.g. the surface density of stars  $\Sigma_{RC}$ , mean distance modulus  $\mu$ , and geometrical variance  $\sigma_\mu$ , with that directly from observation for the model  $E_3$ . In the top left panel of Fig. 2, we plot  $\Sigma_{RC}$  for three stripes at  $|b| = 2.5^\circ, 4.0^\circ, 5.5^\circ$  as observed in Nataf et al. (2013).  $\Sigma_{RC}$  is maximized near  $l = 0^\circ$  for all latitude stripes. In the same figure, we also plot the  $E_3$  model predictions of  $\Sigma_{RC}$ . At small longitudes, the model predictions are consistent with the observations. However, at large longitudes, especially for the  $|b| = 5.5^\circ$  stripe, the model predictions are systematically lower than the observation. In the top right panel of Fig. 2, we plot  $\Sigma_{RC}$  from both model predictions and observations at fixed longitudes of  $l = 0.0^\circ, 5.0^\circ$  and  $10.0^\circ$  respectively. It shows the expected result that number counts increase monotonically with decreased separation from the plane for each longitude. However, it again shows that at large longitude, especially for the  $l = 10.0^\circ$  stripe, the model predictions  $\Sigma_{RC}$  are systematically lower than the observed values.

The middle left panel of Fig. 2 shows the  $E_3$  model (black symbols) and observed (red symbols) mean distance modulus

Model	$R_0$ (kpc)	$x_0$ (kpc)	$y_0$ (kpc)	$z_0$ (kpc)	$\alpha$ (deg)	$\sigma_I$	$\chi_1^2$	$\chi_2^2$	$\chi_3^2$	$\chi_4^2$	$\chi^2/d.o.f$
$G_1$	8.19	1.15	0.48	0.42	31.9	0.11	24267	33383	29546	6015	3.45
$E_2$	8.16	0.69	0.29	0.25	30.4	0.00	16733	31878	19344	1430	2.57
$E_3$	8.12	0.70	0.30	0.28	27.3	0.00	15469	31395	17967	-1474	2.34

**Table 2.** The same as Table 1, but taking the intrinsic dispersion of the RC  $\sigma_I$  as a free parameter.

$\mu$  against longitude. In the middle right panel, we plot  $\mu$  at fixed longitudes of  $l = -5.0^\circ, 0^\circ$  and  $5.0^\circ$ . The bottom panels of Fig. 2 is the same as the top panel, but for the dispersion in distance modulus  $\sigma_\mu$ . The dependence on longitude and latitude is reproduced, but the model prediction does not match the observation perfectly. In particular, for the  $l = 10^\circ$  stripe, the prediction is systematically lower than the observation.

Notice that negative values of  $\sigma_\mu^2$  should not be a cause of concern. Nataf et al. (2013) estimated the dispersion due to geometric extension  $\sigma_\mu^2$  as:

$$\sigma_\mu^2 = \sigma^2 - \sigma_I^2 - \sigma_E^2 \quad (11)$$

where  $\sigma^2$  is the measured brightness dispersion of the RC,  $\sigma_I = 0.09$  is the estimated intrinsic magnitude dispersion of RC, and  $\sigma_E^2$  is the dispersion due to differential extinction. Therefore, for sightlines where the measured brightness dispersion is small relative to the intrinsic dispersion and differential extinction, we can sometimes obtain negative variance in  $\sigma_\mu^2$ . We do not remove these sightlines with negative geometrical variance to avoid systematically biasing the final output to have large variance. However, in the bottom panels of Fig. 2 the predicted  $\sigma_\mu$  are well concentrated while the data have very wide variations. It could be that the models are wrong, or it could be that the data are wrong. To test for the latter, we take the intrinsic dispersion of the RC as a free parameter instead of  $\sigma_I = 0.09$  as quoted in Nataf et al. (2013). The results are presented in Table 2. We can see different values of  $\sigma_I$  are favored for different models: for the  $G_1$  model, the best-fit  $\sigma_I$  is preferred to be 0.11; for models  $E_2$  and  $E_3$ ,  $\sigma_I = 0$  is preferred. The differences in the  $\chi^2$  are formally important. However, since our models do not have  $\chi^2/d.o.f$  close to one, which indicates systematic departures from our smooth ellipsoidal model (e.g., the X-shaped structure), we thus do not regard the inclusions of the additional parameters as very significant (i.e., the value of  $\sigma_I$  is not well constrained by the spatial density models), and thus will not be discussed any further.

In Fig. 3, we plot the mean distance to RC centroids measured by Nataf et al. (2013) and give the  $E_3$  model predictions in the same figure for comparison. The distances are projected onto a face-on view of the central region of the Galaxy. The left panel of Fig. 3 shows data for sightlines with  $2.5^\circ \leq |b| \leq 3.5^\circ$ , while the right panel is for sightlines with  $4.5^\circ \leq |b| \leq 5.5^\circ$ . The model prediction is broadly consistent with the observations, but does not yield a very significant flattening at small positive longitudes as is seen in the data.

An interesting phenomenon, recently discovered, is that the RC of the bulge is observed to show two peaks in distance at large separations from the plane (Nataf et al. 2010; McWilliam & Zoccali 2010; Saito et al. 2011), a result that has been shown to be due to an X-shape structure by means of N-body models (Li & Shen 2012; Ness et al. 2012). The existence of the vertical X-shaped structure hints that the formation of the Milky Way bulge is shaped mainly by internal disk dynamical instabilities.

To verify the X-shaped fine structure, we calculate the excess fraction in star counts between the model and the observed data,  $(N_{\text{obs}} - N_{\text{model}})/N_{\text{model}}$ , for each sightline. We then project the excess fraction to produce a 2-D residual map in the X-Z plane, shown in the top panel of Fig. 4 for the  $E_3$  model. We can see a dim X-shaped structure extending from the x-axis  $\sim 6$  kpc to  $\sim 10$  kpc, with  $|z| \leq 1$  kpc. We observe  $2.94 \times 10^6$  stars, while we find a predicted number of RCs for the bulge of  $2.78 \times 10^6$ , implying an excess RC population of 5.8%. The existence of an X-shape structure suggests that at the outer regions of the bulge, there is some fine structure in the Galactic bar. In the bottom panel of Fig. 4, we project the excess fraction in the l-b plane and verify that the X-shape structure is also apparent in the side-on view.

As mentioned above, we also consider more complex models by introducing the tilt angle  $\beta$ , a centroid offset  $(\delta l, \delta b)$ , and the tilt angle and centroid offset together. To avoid confusion, these models are labelled as  $G'_1, E'_2$  and  $E'_3$ ,  $G''_1, E''_2$  and  $E''_3$ ,  $G'''_1, E'''_2$  and  $E'''_3$ . The fitting results are presented in Table 1. As we mentioned before, while the improvement of  $\chi^2$  due to the additional parameters is formally significant, in light of the large  $\chi^2/d.o.f$  for our best-fit model. we do not pursue these parameters any further. This is reasonable since our sightlines do not cover the plane and very central regions which would presumably show the most prominent deviations from a tilt and non-offset model. Thus from now on  $\beta$ ,  $\delta l$  and  $\delta b$  will all be fixed at zero.

#### 4.1 Disk contamination

There is evidence that there is some structural change in the Galactic bulge inward of  $l \leq 4^\circ$  (Gerhard & Martinez-Valpuesta 2012). As mentioned above, the vertical X-shaped structure is assumed to be shaped mainly by internal disk dynamical



Model	Areas	Sightlines	$R_0$ (kpc)	$x_0$ (kpc)	$y_0$ (kpc)	$z_0$ (kpc)	$\alpha$ (deg)	$\chi_1^2$	$\chi_2^2$	$\chi_3^2$	$\chi_4^2$	$\chi^2/d.o.f$
$G_1$	$ l  \leq 4^\circ$	5995	8.19	1.26	0.42	0.40	29.2	14683	23058	19067	1762	3.26
$E_2$	$ l  \leq 4^\circ$	5995	8.16	0.77	0.24	0.24	31.6	11025	21375	12707	832	2.56
$E_3$	$ l  \leq 4^\circ$	5995	8.14	0.71	0.25	0.27	27.7	9647	20829	10402	734	2.31
$G_1$	$ l  \leq 4^\circ$ and $ b  \leq 4^\circ$	4405	8.19	1.08	0.39	0.37	27.8	8182	18415	11109	280	2.88
$E_2$	$ l  \leq 4^\circ$ and $ b  \leq 4^\circ$	4405	8.16	0.68	0.23	0.25	31.2	7043	16903	8170	-63	2.47
$E_3$	$ l  \leq 4^\circ$ and $ b  \leq 4^\circ$	4405	8.14	0.68	0.25	0.28	28.1	6606	16385	8006	-40	2.34

**Table 3.** The same as Table 1, but removing the outer part of the bulge regions.

instabilities and extend to large distance. Both features are a source of disk contamination which is difficult for our model to reproduce, especially in regions remote from the centre of the bulge. From Fig. 2, we can see that at larger longitude, the number counts and geometrical variance in observation also systematically deviate from the model prediction.

To see the effects of possible disk contamination, we simply exclude data from the outer part of the bulge. We adopt two cut criteria. Firstly, we remove sightlines with  $|l| > 4^\circ$ . Secondly, we retain only the sightlines whose longitude and latitude are both smaller than  $4^\circ$ . The value of 4 degrees is chosen because in this region, there is a slope change in the particle surface density, see, e.g., Fig. 2 of Gerhard & Martinez-Valpuesta (2012).

We test the results of the models for the above two criteria (Table 3). Of course, after excluding the outer part, the resulting region is smaller with respect to the original size of the OGLE-III data. If we exclude the  $|l| > 4^\circ$  areas, there are 5995 sightlines remaining and the area is reduced to  $40.67 \text{ deg}^2$ . Similarly, if we exclude the  $|l| > 4^\circ$  and  $|b| > 4^\circ$  areas, there are 4405 sightlines remaining in  $17.81 \text{ deg}^2$ . Compared with the models for the whole dataset, excluding the outer part of the bulge results in better models in terms of  $\chi^2/d.o.f$  (see Table 3). We present in Figs. 5 and 6 the PDF and contours of the parameters of  $E_3$  when we exclude  $|l| > 4^\circ$  only and both  $|l| > 4^\circ$  and  $|b| > 4^\circ$  respectively. We again calculate the model-predicted RC population, and find the excess is reduced to 3.2% for excluding fields with  $|l| > 4^\circ$  and 2.9% for  $|l| > 4^\circ$  and  $|b| > 4^\circ$ . These are not surprising since as we can see from Figs. 2 and 4 both the larger dispersion and excess lie in the outer region of the bulge. This suggests that we can obtain a more realistic inner bar structure after excluding the large longitude sightlines. The cuts on the data partly avoid the disk contamination and fine structure, which are presently very difficult to handle.

## 4.2 Comparison with results from OGLE-II

Rattenbury et al. (2007) used RCG stars from 44 bulge fields from the OGLE-II microlensing collaboration database to constrain analytical tri-axial models for the Galactic bar. They found the bar major axis is oriented at an angle of  $24^\circ$  to  $27^\circ$  to the Sun-Galactic centre line of sight. They also found the ratio of semi-major and semi-minor bar axis scale lengths in the Galactic plane  $x_0, y_0$ , and vertical bar scale length  $z_0$ , to be  $x_0 : y_0 : z_0 = 1.00 : 0.35 : 0.26$ .

As mentioned in the introduction, the data from OGLE-III as analyzed by Nataf et al. (2013) offer many larger sky coverage and better calibration in the RCG population. Both are helpful to refine the constraints on the bar parameters. We obtain a bar angle oriented at  $29.4^\circ$ , and the axis ratios are around  $x_0 : y_0 : z_0 = 1.00 : 0.43 : 0.40$  with the scale length of the major axis being 0.67 kpc for the  $E_3$  model. The scale length of the major axis is shorter than that found by Rattenbury et al. (2007) (1.00 kpc), while similar to Dwek et al. (1995) (0.69 kpc). This suggests a bulge that is not as tri-axial as that found by Rattenbury et al. (2007). The bar is also vertically more extended than the working model of Gerhard (2002) with  $x_0 : y_0 : z_0 = 1.00 : 0.40 : 0.30$ . We notice that the scale lengths for different models are different, the Gaussian model has the largest scale length among all the models. An exponential falls off more slowly than a Gaussian; it has a longer tail. So to include the same number of stars within some physical scale, an exponential fit will have a smaller scale length than a Gaussian.

When using all the data, we found an excess, consistent with the so-called X-shape structure in the bulge region. The excess is  $\sim 5.8\%$ , approximately in agreement with model of Li & Shen (2012) when evaluated with their method, which complicated the fitting. It is peculiar that the extrema of the X-shaped structure are at the distance of twice the scale length. Its appearance may be perturbed by disk contamination. As shown in Fig. 4, there are fluctuations in the large longitude areas ( $1 \sim 10^\circ$ ), and thus may not be the true excess shown of the X-shaped structure. We remove those regions and keep the fields with  $-4^\circ \leq l \leq 4^\circ$  and  $-4^\circ \leq b \leq 4^\circ$  to address this issue and concentrate on the inner region of the bar. As a result, the effect of the fine structure is reduced and we can fit a smoother inner bar structure.

## 4.3 Comparison with Robin et al. (2012)

The bar angle we measure is larger than the value found by Robin et al. (2012) ( $13^\circ$ ). As they pointed out, the bar angle seems to vary with the range of longitude, latitude and population considered, and is found to be between 10 to 45 degrees.

Model	$R_0$ (kpc)	$x_0$ (kpc)	$y_0$ (kpc)	$z_0$ (kpc)	$\alpha$ (deg)	$\chi_1^2$	$\chi_2^2$	$\chi_3^2$	$\chi_4^2$	$\chi^2/d.o.f$
G <sub>1</sub>	8.23	1.00	0.56	0.43	13.0	44097	74272	35489	15688	6.27
E <sub>2</sub>	8.15	0.51	0.34	0.26	13.0	33056	90302	26821	16804	6.17
E <sub>3</sub>	8.13	0.58	0.33	0.27	13.0	32164	68300	27402	10506	5.12

**Table 4.** The same as Table 1, but fix the bar angle to be  $13^\circ$ .

The parameterization of Robin et al. (2012) is optimized for values of the bar angle  $\alpha$  at the lower end of values found in the literature. The 2MASS data they use have the advantage that it is all-sky, and thus are not limited by spatial coverage. However, 2MASS is also a shallower survey. For most of the bulge, and indeed nearly the entire region we used in our study, 2MASS does not reach the RC population. The upper red giant population has a much broader luminosity range, and a much greater disc contamination fraction, and so we believe RC is a much better tracer of the bulge/bar. Another point is that the study by Robin et al. (2012) removes a lot of data. Their model does not analyze data below the 2MASS completeness limit in J and  $K_s$  (see their §3.2). This implies that they have a variable population under study in every sightline, as the extinction increases, the effective population under study changes a systematic way. In contrast, OGLE-III probes luminosities substantially fainter than the RC over 98% of its survey area, so we are not biased in this manner.

We can further test how the bar angle affects the  $\chi^2$  in our own models by forcing the bar angle to be  $13^\circ$  as advocated by Robin et al. (2012), and optimize all other parameters. The results are presented in Table 4. we find the best-fit  $\chi^2/d.o.f$  is much larger than that without fixing the bar angle. The scale length of the major axis is 1.00, 0.51 and 0.58 kpc for the  $G_1$ ,  $E_2$  and  $E_3$  respectively, which is smaller than 1.18, 0.67, 0.66 kpc when the bar angle is included in the fitting, this is reasonable since the length of the bar decreases with the increase of the orientation angle for a fixed observed bar length.

#### 4.4 Effect of Metallicity

A vertical metallicity gradient has been measured in the bulge (Zoccali et al. 2008; Ness et al. 2013). Currently, the metallicity gradient has only been demonstrated for sightlines far from the plane, for which Ness et al. (2013) find a shallow value of  $\sim 0.07$  dex degree $^{-1}$ . For sightlines closer to the plane, spectroscopic data indicates that the metallicity gradient levels off (Rich et al. 2012). Thus, the metallicity gradient could in principle be a source of systematic error in our investigation, but only for sightlines far from the plane.

We first refer the reader to Salaris & Girardi (2002), who used stellar models to demonstrate that metallicity effects on the RC absolute magnitude are substantially smaller in I-band than in either V-band or K-band, which we argue is one of the principle advantages of studying the bulge in optical data from the OGLE-III photometric survey (Szymański et al. 2011).

We can constrain the impact of population effects as follows. Nataf et al. (2013) used models from the BaSTI stellar database (Pietrinferni et al. 2004) to find that the predicted value of  $dM_{I,RC}/d[M/H] = 0.20$  mag dex $^{-1}$ , and  $d(V - I)_{RC,0}/d[M/H] = 0.27$  mag dex $^{-1}$ . Sightlines with a lower metallicity will thus have a slightly underestimated extinction and a slightly underestimated apparent distance – the two effects nearly cancel. As the mean extinction law for the bulge is  $A_I/E(V - I) = 1.22$ , the distance error works out to 0.13 mag in distance modulus per dex of metallicity. As the metallicity variation across our fields should be no greater than 0.2 dex, this works out to a potential distance error of 1.0%. In contrast, the systematic variation in distance due to the Galactic bar’s orientation is 20%.

The relative impact of population effects on  $N_{RC}$  is even smaller. Girardi & Salaris (2001) compute the predicted number of RC stars in a stellar population as a function of its age and metallicity, which they show in their Figure 1 and summarize in their Table 1. For ages greater than 6 Gyr, the predicted differences for  $[Fe/H] = -0.3, 0.0, \text{ and } +0.20$  (characteristic metallicities for the bulge) are or order 3%. In contrast, the variation in number counts in the fields studied in this work exceeds 600%, due to the spatial density profile of the bulge. The systematic error is thus smaller than 1 part in 100.

We thus conclude that our study should not be sensitive to population effects. They do exist, but they are not large. Inclusion of these effects would actually be likely to reduce the quality of our analysis, as they are not adequately characterised across the bulge.

## 5 SUMMARY AND DISCUSSION

We use the RCG population in the OGLE-III database to fit a tri-axial Galactic bar model and to derive much tighter constraints on the bar parameters. When using all the available data, we found there is evidence for an X-shaped structure in the outer part of the bulge region, with observable properties consistent with those of Li & Shen (2012). This fine structure complicated the fitting of our analytic models. We removed data from the area in the outer part of the bulge region and retained the fields with  $-4^\circ \leq l \leq 4^\circ$  and  $-4^\circ \leq b \leq 4^\circ$  to partly remove disk contamination and to concentrate on the inner region of the bar. This reduced the effect of the fine structure and allowed a fit to the resulting smoother inner bar structure.

We find that the bar prefers the  $E_3$  model and has a bar angle of  $29.4^\circ$ . We measure the scale length of major axis of 0.67 kpc with an axis ratio of  $x_0 : y_0 : z_0 = 1.00 : 0.43 : 0.40$  for the  $E_3$  model. This bar is close to being prolate, and not as triaxial as the bar structure found by Rattenbury et al. (2007); it appears vertically thicker than the working model of Gerhard (2002) who gives  $x_0 : y_0 : z_0 = 1.00 : 0.40 : 0.30$ . For the best fit  $E_3$  model, the predicted total number of RCGs for the bulge is  $1.05 \times 10^7$ . Following the method outlined in Nataf et al. (2013), we estimate the total bar stellar mass is  $1.8 \times 10^{10} M_\odot$ , about 10% lower but more accurate than that in Nataf et al. (2013).

The model derived here can effectively reproduce the number density, distance modulus over the sky probed by the OGLE-III data (Nataf et al. 2013). Future microlensing observations will provide us with additional constraints on the structure of the Galactic bar. Based on the improved and tightly constrained bar model, it will be interesting to re-calculate the optical depths and time-scale distribution for microlensing events, and see whether they are consistent with the data.

The X-shaped structure appears in both simulations and in our data. Its existence in the Milky way implies that the Galactic bulge is shaped mainly by internal disk dynamical instabilities instead of mergers (e.g. Li & Shen 2012). How to model subtle structures such as the X-shaped excess remains a challenging task. One possible way forward is to expand the density distribution into orthogonal basis functions; a similar approach is taken in weak lensing to model complex point spread functions (Andrae et al. 2011); we plan to explore this in the near term.

## ACKNOWLEDGMENTS

We acknowledge the National Astronomical Observatories (NAOC) and Chinese Academy of Sciences (CAS) for financial support (SM). LC acknowledges the support of the NSFC grant (11203028) and the Young Researcher Grant of NAOC. This work is also made possible through the support of a grant from John Templeton Foundation (LC). Andrew Gould acknowledges the NSF grant (AST-1103471) and is also partly supported by a senior visiting professorship of CAS. We thank Drs. Lia Athanassoula, Junqiang Ge, Ortwin Gerhard and Guoliang Li for helpful discussions and Dr. Radek Poleski for comments.

## REFERENCES

- Andrae, R., Melchior, P., & Jahnke, K. 2011, *MNRAS*, 417, 2465  
 Athanassoula, E. 2012, arXiv:1211.6752  
 Babusiaux, C., Gilmore, G., 2005, *MNRAS*, 358, 1309  
 Binney, J., Gerhard, O.E., Stark, A.A., et al., 1991, *MNRAS*, 252, 210  
 Blitz, L., Spergel, D.N., 1991, *ApJ*, 379, 631  
 Dwek, E., Arendt, R.G., Hauser, M.G., et al., 1995, *ApJ*, 445, 716  
 Dunkley, J., Bucher, M., Ferreira, P. G., Moodley, K., & Skordis, C. 2005, *MNRAS*, 356, 925  
 Freeman, K., Ness, M., Wylie-de-Boer, E., et al. 2013, *MNRAS*, 428, 3660  
 Gerhard, O., 2002, in G.S. Da Costa, H. Jerjen, eds., *ASP Conf. Ser. 273: The Dynamics, Structure & History of Galaxies: A Workshop in Honour of Professor Ken Freeman*, 73  
 Gerhard, O., & Martinez-Valpuesta, I. 2012, *ApJ*, 744, L8  
 Girardi, L., & Salaris, M. 2001, *MNRAS*, 323, 109  
 Gonzalez, O. A., Rejkuba, M., Minniti, D., et al. 2011, *A&A*, 534, L14  
 Hastings, W.K. 1970, *Biometrika* 57,97  
 Howard, C. D., Rich, R. M., Reitzel, D. B., et al. 2008, *ApJ*, 688, 1060  
 Lewis, A., & Bridle, S. 2002, *Phys. Rev. D*, 66, 103511  
 Li, Z.-Y., & Shen, J. 2012, *ApJ*, 757, L7  
 Long, R. J., Mao, S., Shen, J., & Wang, Y. 2013, *MNRAS*, 428, 3478  
 McWilliam, A., & Zoccali, M. 2010, *ApJ*, 724, 1491  
 Metropolis, N.; Rosenbluth, A.W.; Rosenbluth, M.N.; Teller, A.H.; Teller, E. 1953. *Journal of Chemical Physics* 21, 1087  
 Nakada, Y., Onaka, T., Yamamura, I., et al., 1991, *Nature*, 353, 140  
 Nataf, D. M., Udalski, A., Gould, A., Fouqué, P., & Stanek, K. Z. 2010, *ApJ*, 721, L28  
 Nataf, D. M., Gould, A., Fouqué, P., et al. 2013, *ApJ*, 769, 88  
 Ness, M., Freeman, K., Athanassoula, E., et al. 2012, *ApJ*, 756, 22  
 Ness, M., Freeman, K., Athanassoula, E., et al. 2013, *MNRAS*, 430, 836  
 Nidever, D. L., Zasowski, G., Majewski, S. R., et al. 2012, *ApJ*, 755, L25  
 Nishiyama, S., Nagata, T., Baba, D., et al., 2005, *ApJ*, 621, L105  
 Pietrinferni, A., Cassisi, S., Salaris, M., & Castelli, F. 2004, *ApJ*, 612, 168  
 Rattenbury, N. J., Mao, S., Sumi, T., & Smith, M. C. 2007, *MNRAS*, 378, 1064



- Rich, R. M., Origlia, L., & Valenti, E. 2012, *ApJ*, 746, 59
- Robin, A. C., Marshall, D. J., Schultheis, M., & Reyl e, C. 2012, *A&A*, 538, A106
- Salaris, M., & Girardi, L. 2002, *MNRAS*, 337, 332
- Saito, R. K., Zoccali, M., McWilliam, A., et al. 2011, *AJ*, 142, 76
- Sellwood J. A., Wilkinson A., 1993, *RPPh*, 56, 173
- Stanek, K.Z., Mateo, M., Udalski, A., et al., 1994, *ApJ*, 429, L73
- Stanek, K.Z., Udalski, A., Szymanski, M., et al., 1997, *ApJ*, 477, 163
- Su, M., & Finkbeiner, D. P. 2012, arXiv:1206.1616
- Szymański, M. K., Udalski, A., Soszyński, I., et al. 2011, *Acta. Astronom.*, 61, 83
- Terndrup, D. M., Popowski, P., Gould, A., Rich, R. M., & Sadler, E. M. 1998, *AJ*, 115, 1476
- Udalski, A., Szymanski, M., Stanek, K.Z., et al., 1994, *Acta Astronomica*, 44, 165
- Wang, Y., Zhao, H., Mao, S., & Rich, R. M. 2012, *MNRAS*, 427, 1429
- Weiland, J.L., Arendt, R.G., Berriman, G.B., et al., 1994, *ApJ*, 425, L81
- Zoccali, M., Hill, V., Lecureur, A., et al. 2008, *A&A*, 486, 177

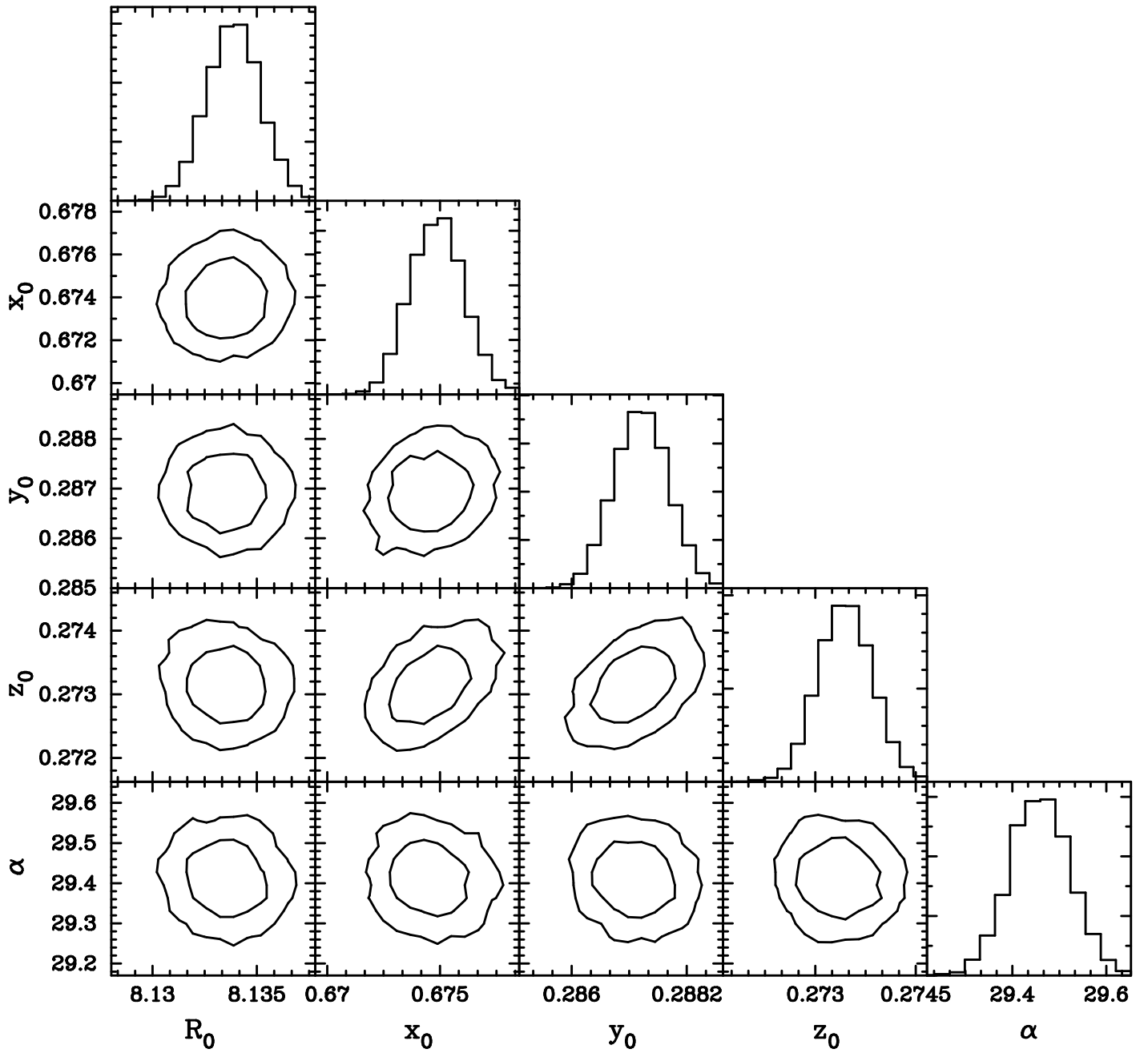


**Figure 1.** The marginalised probability density distributions (PDFs) and contours in the plane of  $R_0$ ,  $x_0$ ,  $y_0$ ,  $z_0$ ,  $\alpha$  for the six-parameter  $E_3$  model. All the lengths are in units of kpc and the angle  $\alpha$  is measured in degrees. The inner and outer contours are respectively for the 1- $\sigma$  and 2- $\sigma$  confidence level regions (for two parameters simultaneously).

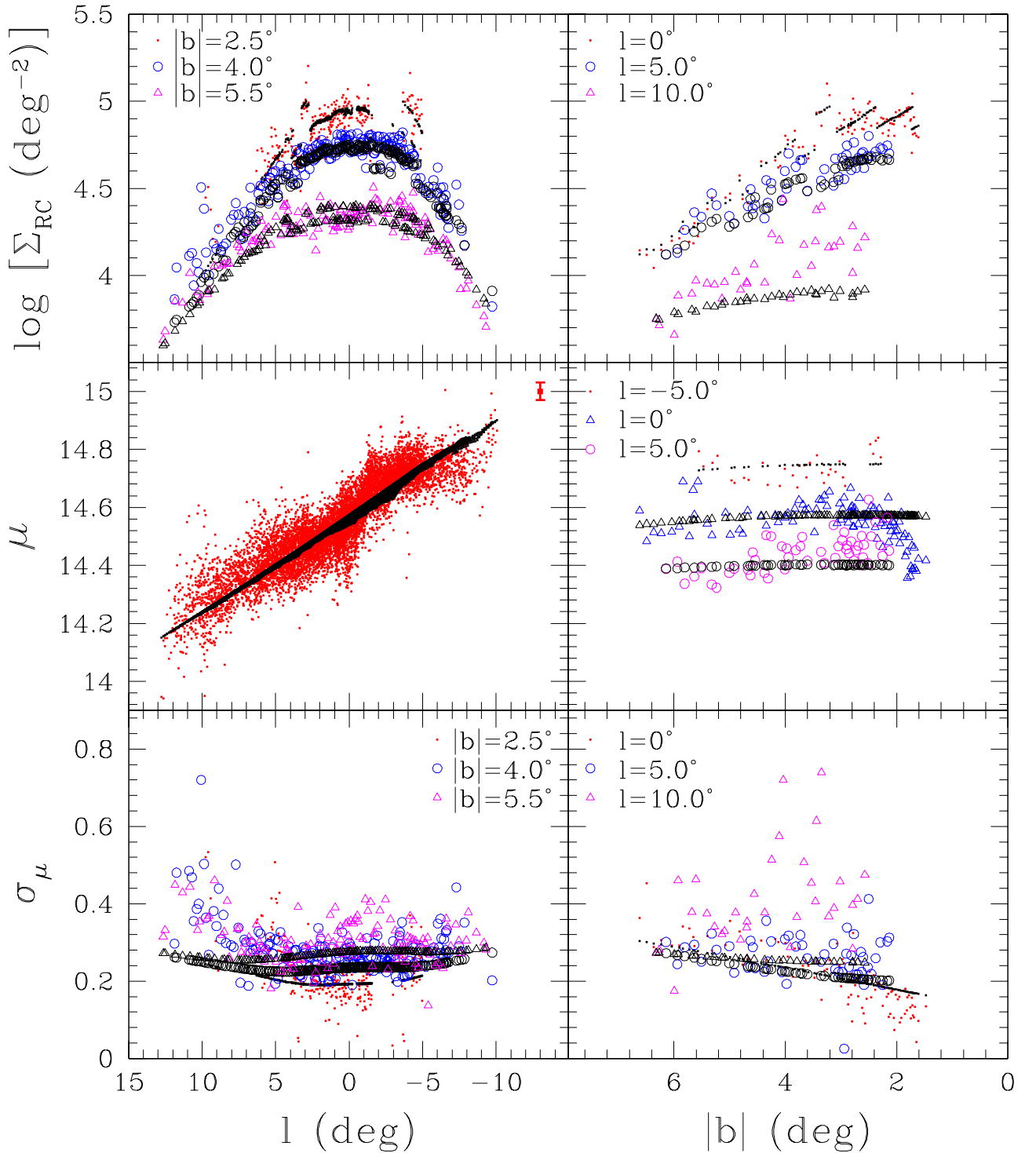


**Figure 2.** The predicted surface density of stars  $\Sigma_{RC}$ , mean modulus  $\mu$ , and dispersion in modulus  $\sigma_\mu$ , vs. those directly from observation  $E_3$  model. Top panels: the surface number density  $\Sigma_{RC}$  vs. longitude (left) and latitude (right). Middle panels: mean distance modulus  $\mu$  vs. longitude (left) and latitude (right). Bottom panels: dispersion in modulus  $\sigma_\mu$  vs. longitude (left) and latitude (right). In all panels, black symbols denote model values while colour symbols denote observational data. The point with error bar at middle left panel is the median error on the measurement reported by Nataf et al. (2013).

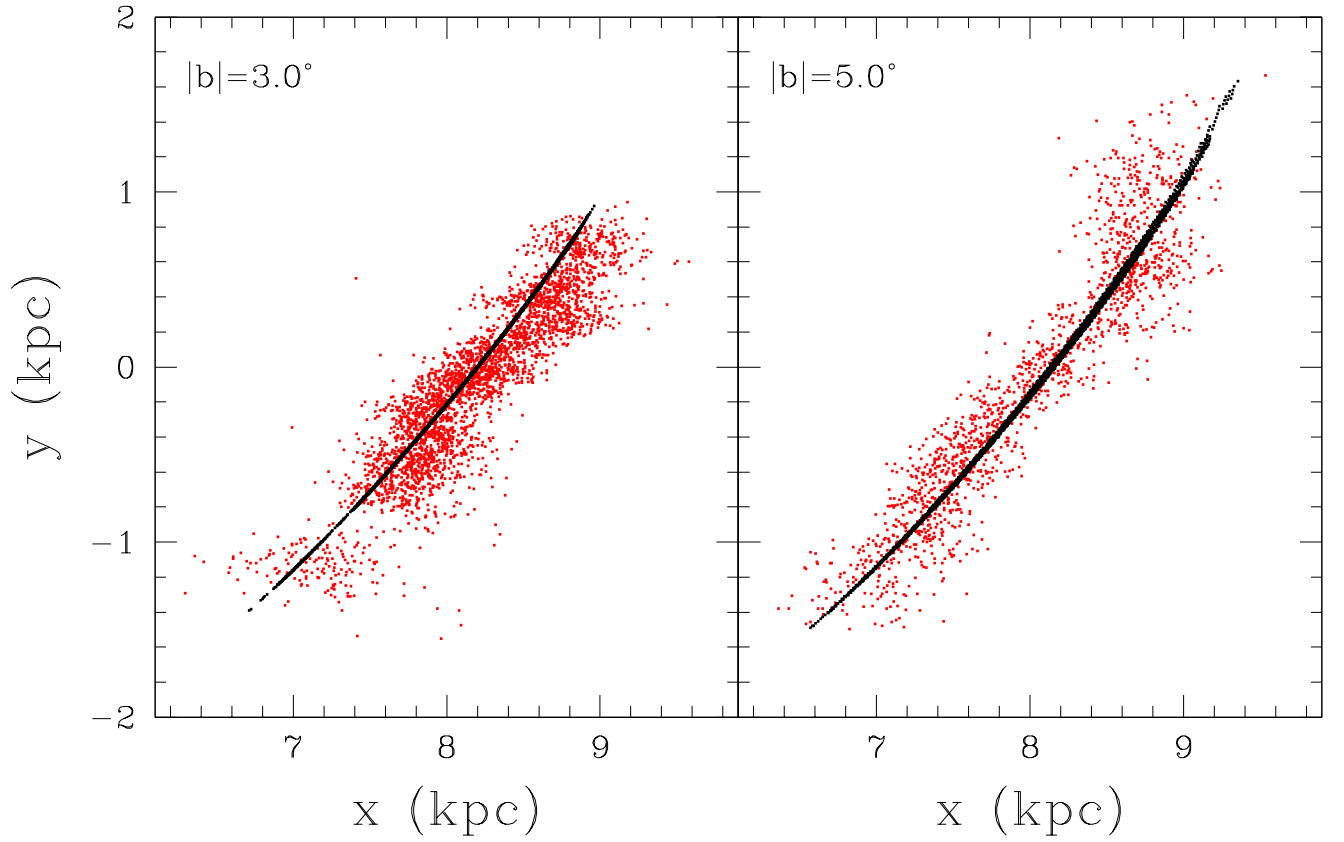


**Figure 3.** The face-on view projection of the distances to RC centroids for the  $E_3$  model. The red points show the projected location of each measured RC centroid, and black points show the model prediction. The left panel is for sightlines satisfying  $2.5^\circ \leq |b| \leq 3.5^\circ$ , while the right panel is for  $4.5^\circ \leq |b| \leq 5.5^\circ$  sightlines.

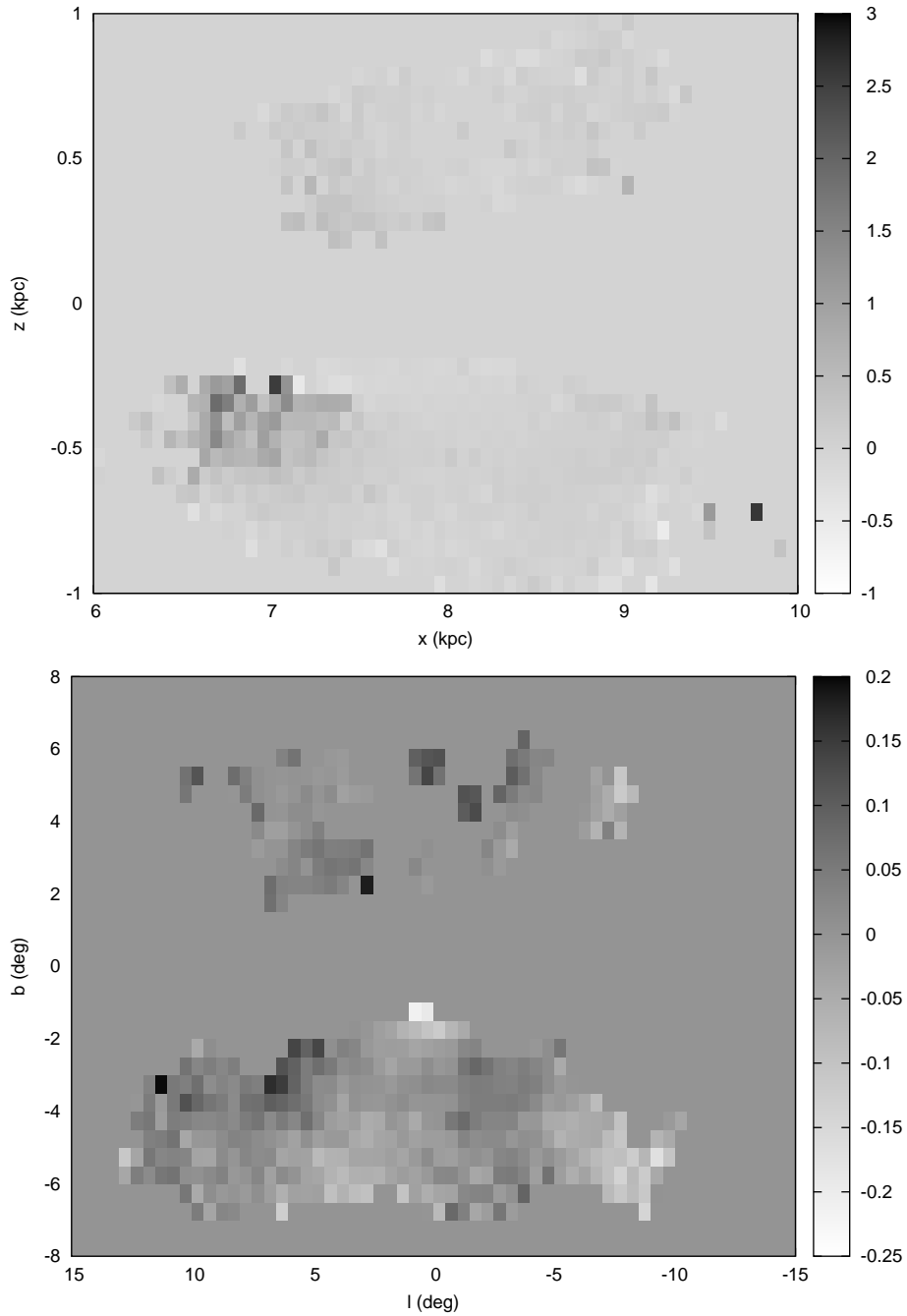


**Figure 4.** The residual map of number counts for the six-parameter  $E_3$  model for edge-on (top) and side-on view (bottom) respectively. The residual of number counts is defined as the fractional difference in star counts between the model and the observed data,  $(N_{\text{obs}} - N_{\text{model}})/N_{\text{model}}$ . The total excess fraction of number counts is 5.8%.



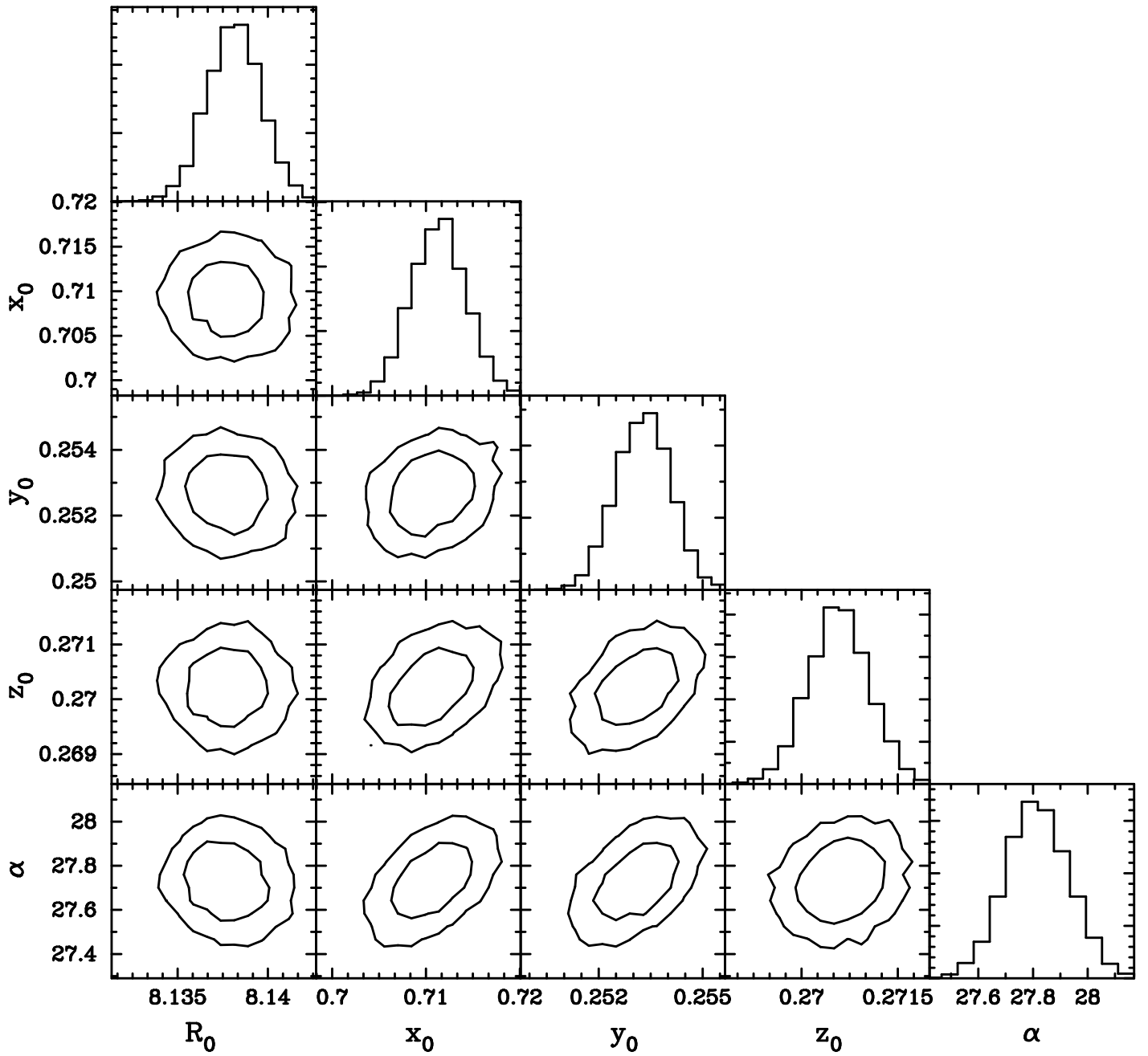


Figure 5. The same as Fig. 1, but after excluding the  $|l| > 4^\circ$  areas.

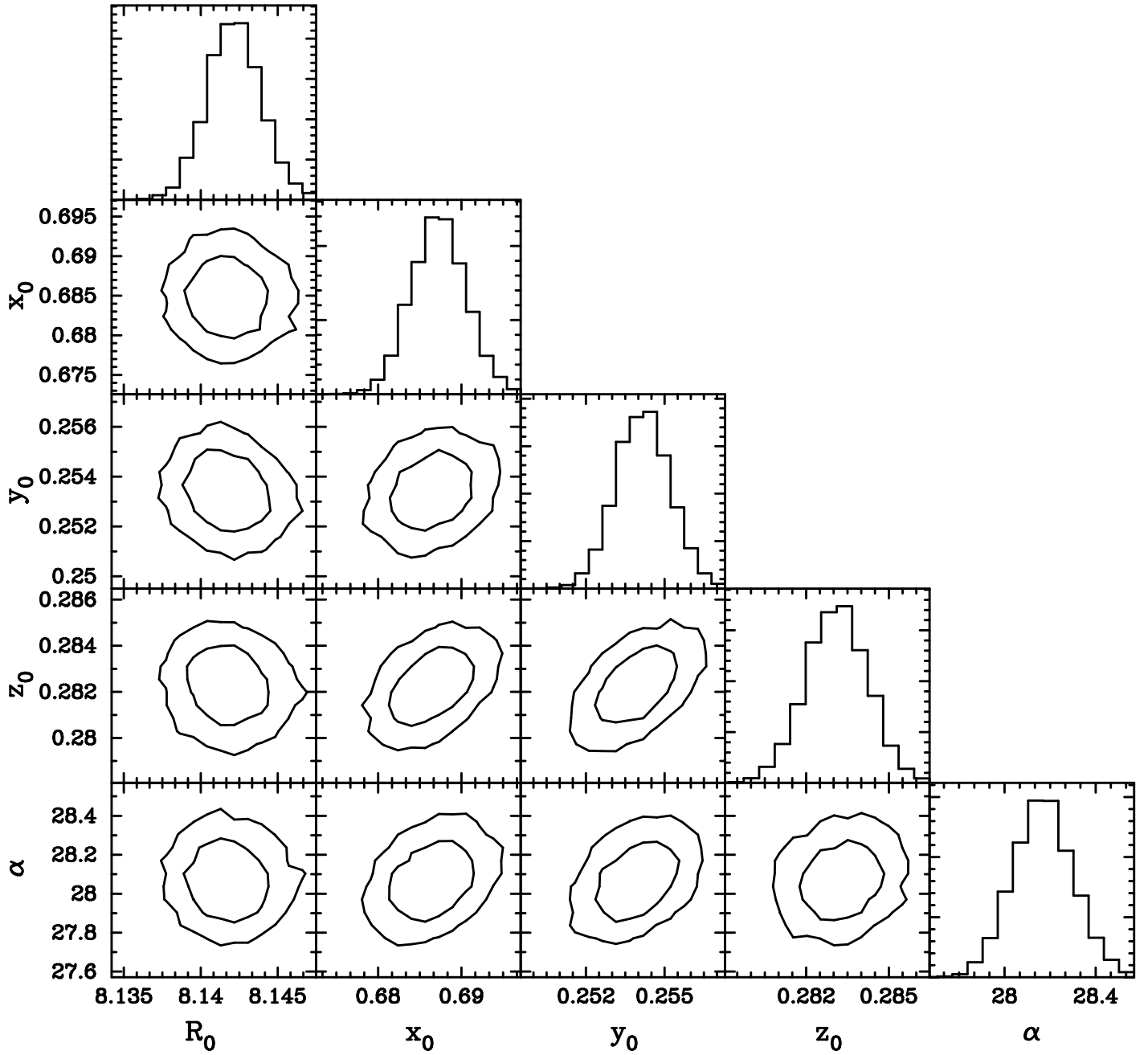


Figure 6. The same as Fig. 1, but after excluding the  $|l| > 4^\circ$  and  $|b| > 4^\circ$  areas.